The luminosity dependence of thermally-driven disc winds in X-ray binaries

Nick Higginbottom,[1][*] Christian Knigge[1], Knox S. Long[2,3], James H. Matthews[4] and Edward J. Parkinson[1].

[1] *School of Physics and Astronomy, University of Southampton, Highfield, Southampton, SO17 1BJ, UK*
[2] *Space Telescope Science Institute, 3700 San Martin Drive, Baltimore, MD, 21218, USA*
[3] *Eureka Scientific Inc., 2542 Delmar Avenue, Suite 100, Oakland, CA, 94602-3017, USA*
[4] *University of Oxford, Astrophysics, Keble Road, Oxford OX1 3RH, UK*
[5] *School of Mathematics and Physics, Queen's University Belfast, University Road, Belfast BT7 1NN, UK*

ABSTRACT

We have carried out radiation-hydrodynamic simulations of thermally-driven accretion disc winds in X-ray binaries. Our main goal is to study the luminosity dependence of these outflows. The simulations span the range $0.04 \leq L_{acc}/L_{Edd} \leq 1.0$ and therefore cover most of the parameter space in which disc winds have been observed. We find that (i) the wind *efficiency* always remains approximately constant at $\dot{M}_{wind}/\dot{M}_{acc} \simeq 2$; (ii) the wind velocity – and hence the maximum blueshift seen in wind-formed absorption lines – increases with luminosity; (iii) the large-scale wind geometry is quasi-spherical, but observable absorption features are preferentially produced along high-column equatorial sightlines. We also present synthetic Fe XXV and Fe XXVI absorption line profiles for our simulated disc winds in order to illustrate the observational implications of our results.

Key words: Accretion discs – hydrodynamics – methods:numerical – stars:winds – X-rays:binaries

1 INTRODUCTION

Signatures of outflowing gas have been observed in essentially all types of disk-accreting astrophysical systems, from protostars, cataclysmic variables and X-ray binaries to Seyfert Galaxies and Quasars. Highly collimated fast jets are often the most spectacular type of outflow from these systems. However, less collimated, slower and more higly mass-loaded disk winds are at least as common and can actually have a more significant impact, both on the environments of these systems and on the accretion flow itself.

X-ray binaries (XRBs) are systems in which secondary star transfers mass to a compact primary (either a black hole or a neutron star) via an accretion disk. They are excellent laboratories in which to study the accretion physics, with lessons learned from XRBs often finding application also in AGN and other systems (Uttley & McHardy 2001; Maccarone et al. 2003; Falcke et al. 2004; Körding et al. 2006, 2008; Scaringi et al. 2012, 2013; Scaringi 2014; Scaringi et al.

2015; Van de Sande et al. 2015; Aranzana et al. 2018). In particular, XRBs exhibit dramatic changes in their spectra and luminosity over timescales on the order of days (e.g. Sobczak et al. 1999; Park et al. 2004), which can be linked to changes in the nature of the accretion flow (e.g. Nowak 1995; Fender & Belloni 2012). Disk winds are seen when systems are in the "high-soft" state, during which the accretion disk is thought to extend all the way to the central compact object (Ponti et al. 2012, although see Homan et al. 2016). Disc wind signatures are not generally observed in the "low-hard" state, during which the inner disk appears to be truncated, and the X-ray emission is dominated by a Comptonised corona. This suggests that disc winds might play a role in regulating – and perhaps triggering – state changes in XRBs. In fact, for sufficiently high mass-loss rates, disc winds are *expected* to destabilize a steady accretion flow through the disc (Shields et al. 1986).

We are therefore interested in developing a theoretical model for these disk winds, with an eye to predicting their mass-loss rates and hence testing the possibility that they are indeed responsible for state changes. Unfortunately, even the basic driving mechanism for these disk winds remains a

topic of much debate and active research. However, broadly speaking, there are three main contenders – radiation driving, thermal driving, and magneto-hydrodynamic driving.

The first mechanism, radiation driving, involves the transfer of momentum from the radiation field to outflowing matter. This transfer can take place via Compton scattering or via the scattering of (mainly UV) photons by bound-bound transitions. If the ionisation state of the gas is favourable, the latter "line-driving" mechanism can produce a radiation pressure more than $1000\times$ higher than that due to Compton scattering (Castor et al. 1975; Gayley 1995). In X-ray binaries, the observed absorption lines suggest that the outflow is highly ionised (e.g. Kallman et al. 2009; Allen et al. 2018), with an ionization parameter $\xi \geq 3$ (Díaz Trigo & Boirin 2016). In such an environment, line-driving is unlikely to be important. However, the luminosity of some XRBs can approach or even exceed the Eddington limit, so radiation driving via Compton scattering alone may be sufficient to drive – or at least affect – the outflow.

The second mechanism, thermal driving, produces outflows whenever gas is heated to a temperature at which the thermal velocity exceeds the local escape velocity. In this situation, mass-loss is inevitable. This mechanism is particularly attractive in X-ray binaries, where the high-energy radiation emitted close to the accretor can irradiate the outer disk, producing a high-temperature surface layer in which thermal speeds can exceed the escape velocity. As a rule of thumb, thermal winds might be expected to arise at or just inside the Compton Radius (R_{IC}) - the radius at which gas at the Compton temperature (T_C - the temperature at which the Compton heating and cooling rates balance) for a given source SED corresponds to a thermal velocity in excess of the escape velocity (Begelman et al. 1983). More specifically, R_{IC} is given by

$$R_{IC} = \frac{GM_{BH}\mu m_H}{k_B T_C}, \tag{1}$$

where M_{BH} is the mass of the central object, μ is the mean molecular mass (which we set to 0.6), and the other symbols have the usual meaning. For our SED, $T_C = 1.4 \times 10^7$ K, so $R_{IC} = 4.82 \times 10^{11}$ - about 4.6×10^5 gravitational radii.

The third mechanism for driving winds from accretion disks is magnetohydrodynamic in nature. In the presence of a sufficiently strong, large-scale magnetic field, an outflow can be driven from the disk by the magnetic pressure gradient or by centrifugal forces, depending on the geometry of the field. Centrifugal forces can be dominant when the magnetic field is inclined by at least $30°$ with respect to the disc axis. In such an outflow, ionized material is loaded onto the magnetic field lines and accelerated like a bead on a wire as it is forced to co-rotate with the field out to the Alfvén radius. Observations of the disk-wind in GRO J1655-40 in a peculiar 'hypersoft' state suggested that the wind in that case arose well inside R_{IC}. Since the luminosity of the system was thought to be well below the Eddington limit at the time, it was argued that this outflow was likely to be magnetically driven (Stone & Norman 1992; Miller et al. 2006, 2008; Kallman et al. 2009, but also see Netzer 2006; Uttley & Klein-Wolt 2015; Shidatsu et al. 2016).

In reality, all three mechanisms are likely at play simultaneously, perhaps changing in relative importance depending on the geometry and accretion state of the source in question. Of the three mechanisms, thermal driving is particularly interesting in X-ray binaries, because it is almost certain to operate on some level whenever a sufficiently large disk is subjected to strong X-ray irradiation. Indeed, this mechanism might not only be important in X-ray binaries but also in protoplanetary systems (e.g. Owen et al. 2012) and AGN (e.g. Bu & Yang 2018).

The existence of thermally driven outflows from accretion disks has been postulated since such disks were themselves first considered (Shakura & Sunyaev 1973). The first detailed theoretical analysis was carried out by Begelman et al. (1983). This was further developed by Shields et al. (1986), who suggested that the associated mass loss could be sufficient to destabilise the disk. More recently, hydrodynamic simulations have confirmed the viability of this driving mechanism and have also shown that the resulting outflows can produce detectable observable blue-shifted absorption features (Woods et al. 1996; Netzer 2006; Luketic et al. 2010; Higginbottom & Proga 2015).

In principle, thermal driving can drive very high mass-loss rates. However, in practice, the actual mass-loss rate in X-ray heated ouflows depends strongly on the heating and cooling rates in the irradiated gas(Higginbottom et al. 2017). These rates, in turn, depend critically not just on the source SED (Dyda et al. 2017), but also on the position- and frequency-dependent attenuation of the radiation field by material between the source and the wind launching region. This attenuation represents a non-linear coupling between the the outflow and the radiation field, which cannot be captured in standard hydrodynamic simulations.

In an effort to improve on this, we have coupled the radiative transfer code PYTHON to the hydrodynamics code ZEUS. This allows us to carry out the first *radiation-hydrodynamic* (RHD) simulations of thermally driven disk winds. In our initial benchmark RHD calculation (Higginbottom et al. 2018, hereafter H18), attenuation sigificantly reduced the thermally-driven mass-loss rate, although the outflow still carried away mass at more than twice the accretion rate onto the central object. In addition, reasonable agreement was found between synthetic H- and He-like Lyman α lines of Fe generated from the simulation and those seen in *Chandra* observations of the LMXB GRO J1655-40 in the soft-intermediate state.

For the benchmark RHD simulation presented in H18, we adopted an X-ray luminosity of 4% of the Eddington luminosity (L_{Edd}) for a 7 $M_{\odot}$ central black hole. This very much represents the low end of the luminosity range in which disk winds have been observed, with the upper end corresponding to $\simeq L_{Edd}$ (Ponti et al. 2012, hereafter P12). It is therefore clearly important to ask whether and how the properties of these outflows depend on the accretion luminosity. For example, observations suggest that the wind efficiency – by which we mean the ratio of the mass-loss rate to the accretion rate onto the central object – may increase with luminosity, (P12, although this relationship is driven by observations of a single exceptional source). Conversely, recent theoretical work on thermally-driven disk winds has found that the wind efficiency should tend to a roughly constant value (Done et al. 2018, hereafter D18).

Here, we extend our RHD simulations to higher luminosities in order to study the impact of this parameter on key outflow properties, such as the wind mass-loss rate, effi-

ciency, geometry and velocity. As discussed in Section 2, we use the same technique as in H18, with only slight modifications. We present our results in Section 4.4, before making comparisons to observations and earlier theoretical work in Section 4.

2 METHOD

As in H18, we use an operator splitting method to link the hydrodynamic code ZEUS (Stone & Norman 1992, extended by Proga et al. 2000) to our own ionization and radiative transfer code PYTHON[1] (Long & Knigge 2002, extended by Higginbottom et al. 2013 and Matthews et al. 2015). Thermally driven winds are expected to operate only beyond $\simeq 0.1 R_{IC}$, which is independent of the source luminosity. We therefore leave the simulation geometry unchanged from H18 and simply increase the luminosity of the central source. We adopt the same logarithmic grid as in H18, the parameters of which are given in the upper part of Table 1. We use a constant density boundary condition at $z = 0$, providing mass reservoir for any resulting outflow.

The value of this constant density is important, because it determines whether the simulation grid captures the entire acceleration zone of the outflow. X-ray irradiated material in the disk atmosphere can only achieve thermal equilibrium at $T \simeq$ (a few) $\times 10^4$ K (where line/recombination cooling balances photoionization heating) or at $T \simeq 10^{6-7}$ K (where Compton processes dominate). The intermediate temperature region is thermally unstable. The cool branch is only available at low ionization parameters, $\xi = (4\pi F_{irr})/n < \xi_{cool,max}$, where F_{irr} is the incident irradiating flux and n is the density. In order to attain the high temperatures necessary to launch a thermally driven winds, material in the the disk atmosphere must therefore reach and exceed $\xi_{cool,max}$. Such gas becomes thermally unstable and heats up rapidly. In doing so, it expands, driving the wind.

In order to fully capture the acceleration zone of the flow, we have to ensure that, at each disk radius, at least some material with $\xi \leq xi_{cool,max}$ is included in the grid. In the optically thin limit, $F_{irr} = L_X/(4\pi R^2)$, we can ensure this simply by setting the mid-plane density to $n = L_X/(\xi_{cool,max}R^2)$. The mid-plane then corresponds exactly to the bottom of the acceleration zone. This is optimal, because it also avoids the inclusion of static material in the simulation and maximizes the numerical resolution in the acceleration zone.

However, in the RHD simulations presented here, $F_{irr} \neq L_x/(4\pi R^2)$, since the radiation field incident on a given cell has not just undergone geometric dilution, but also attenuation by intervening material. It is therefore not possible to compute the ionization parameter for each mid-plane cell a-priori, since it depends not only on the local density, but also on the density of the developing wind along the sightline back to the central source. We therefore conservatively set the mid-plane density to the value obtained for the optically thin ionisation parameter. This guarantees that our simulations capture the full acceleration zone, at

Luminosity (L_{edd})	0.04	0.1	0.3	0.6
Physical Parameters				
M_{BH} ($M_\odot$)	7	7	7	7
T_x (10^7 K)	5.6	5.6	5.6	5.6
L_x (10^{37} ergs s^{-1})	3.3	8.25	24.75	49.5
$\dot{M}_{acc}$ (10^{17} ergs s^{-1})	4.42	11.1	33.2	66.3
$\log(\xi_{cold,max})$	1.35	1.35	1.35	1.35
$T_{eq}(\xi_{cold,max})$ (10^3 K)	50.7	50.7	50.7	50.7
ρ_0 (10^{-12} g cm^{-3})	16.0	40	120	240
R_{IC} (10^{11} cm)	4.82	4.82	4.82	4.82
Derived wind properties				
V_r ($\rho > 1 \times 10^{12}$)				
max, blueshifted (km s^{-1})	50	68	256	150
V_r(max, $\theta > 60°$) (km s^{-1})	259	374	533	642
N_H (70°) (10^{22} cm^{-2})	2.0	4.0	8.3	13
N_H (80°) (10^{22} cm^{-2})	4.2	8.4	16	25
$\dot{M}_{wind,outer}$ (10^{18} g s^{-1})	1.1	2.7	6.7	12.7
$\dot{M}_{wind,outer}$ ($\dot{M}_{acc}$)	2.5	2.4	2.0	1.9
$0.5\dot{M}V_r^2$ (10^{32} erg s^{-1})	4.2	21.3	109	310

Table 1. Parameters adopted in the simulations, along with key properties of the resulting outflows.

the cost of including a small wedge of static material in the grid. The resulting mid-plane densities used in our simulations are given in Table 1.

All other aspects of the simulation are identical to that described by H18, including a truncation of the mid-plane density boundary condition at $R = 2R_{IC}$.

3 RESULTS

We have computed new disk-wind models for central source luminosities in the range $L = 0.1 \, L_{Edd} - 1.0 \, L_{Edd}$ in steps of $0.1 \, L_{Edd}$. To these, we add our original $L = 0.04 \, L_{Edd}$ simulation.

All of our simulations reach stable states, with static disk-like wedges forming at the base of the grid As explained in H18, the reason for this structure is the attenuation of the radiation field by the disk atmosphere. This attenuation increases with radius, causing the ionization parameter in the mid-plane of the simulation to drop. As a result, the vertical height at which $\xi_{cool,max}$ is reached increases with radius. Since this height marks the effective boundary between the static disk and the outflow, the net effect is a thin, slightly convex disk structure.

Since the mid-plane density in our simulations scales with the central source luminosity, the column through the disk atmosphere to a given radius in the mid-plane depends on the luminosity. As a result, the exact shape of the static disk structure also changes slightly with luminosity. In all simulations, the disk/wind interface at the inner edge of the radial grid occurs at around 89° from the z-axis (i.e. 1° above the mid-plane). For our $L = 0.04 L_{Edd}$ simulation, this angle decreases to about 88° at the outer edge; in the $L = L_{Edd}$ simulation, the disk-wind interface at the outer edge of the disk lies at an angle of 87°.

Density contour plots for some of the resulting outflows are shown in Figure 1. Some key parameters summarizing
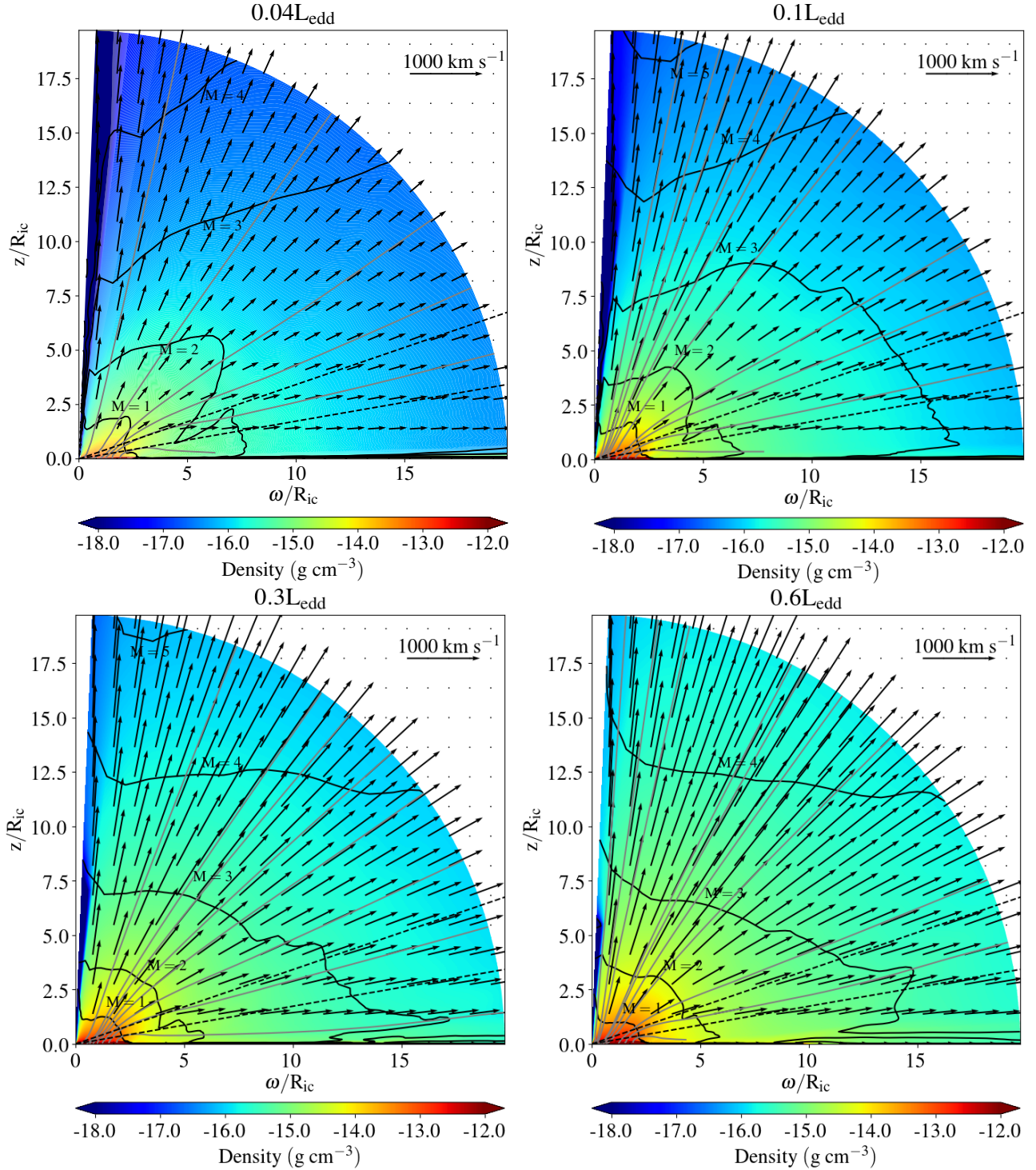
Figure 1. The density (colours) and velocity structure (arrows) of the stable final states for four different luminosities. Grey lines show streamlines, and the black line shows the location of the Mach surfaces. The two dotted lines show the location of the 70° and 80° sightlines.

the character of the outflows are given in the lower part of Table 1. Here and elsewhere, we focus mainly on the results for luminosities $L \lesssim 0.6L_{Edd}$. This is because our simulations do not include radiation driving, a process that would become increasingly important as the luminosity approaches L_{Edd}.

Figure 1 clearly shows that the outflow velocity increases with luminosity, as does the density at a given point in the wind. As one would expect, the mass-loss rate through the outer boundary, which is essentially a function of these two parameters, also increases with luminosity. It is also worth noting that the density and velocity fields in Figure 1
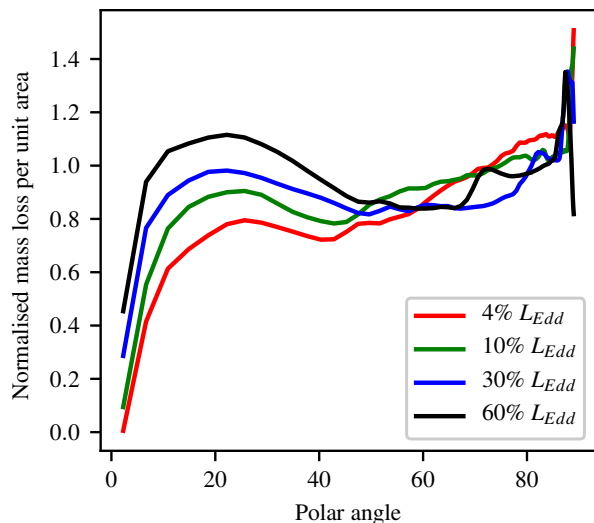
Figure 2. The normalized mass-loss rate per unit area as a function of polar angle. Note that, regardless of luminosity, there is no dramatic increase in this quantity towards high inclinations. On large scales, these outflows are therefore *not* strongly equatorial, but rather quasi-spherical.

do not look particularly equatorial. In the following section, we will consider these critical outflow properties in more detail.

4 DISCUSSION

4.1 Outflow Geometry

Wind-formed X-ray absorption lines have so far only been observed in systems viewed close to edge-on, and this has been interpreted as evidence for an *equatorial* outflow geometry (Ponti et al. 2012, e.g.). Yet, as noted above, Figure 1 does not suggest an equatorial geometry for our simulated disk winds.

We can quantify the outflow geometry by considering how the mass-loss rate per unit area depends on polar angle. This is plotted in Figure **??**, for the full range of luminosities covered by our calculations. As suggested by Figure 1, all of our thermally driven winds are essentially quasi-spherical. Except for a narrow $\theta \lesssim 10°$ "funnel" near the axis, the mass-loss rate per unit area remains almost constant with polar angle. If the outflows were strongly equatorial, we would instead expect the mass-loss rate per unit area to increase strongly towards large polar angles.

This quasi-spherical nature of thermally driven disk winds should actually come as no surprise. After all, the driving mechanism is simply thermal expansion, with no intrinsically preferred direction. On large scales, therefore, *any* thermally driven outflow should be (quasi-)spherical.

So is the geometry of thermally driven disk winds in conflict with observations? The answer is no. Even though the mass-loss rate does not vary strongly with polar angle, the column density through the wind – and hence the equivalent width of the wind-formed lines – do. This is confirmed

in Figure **??**, which shows the predicted EWs for the Fe XXV (1.85 Å) and Fe XXVI Lyman α (1.85 Å) resonance lines (see Section 4.3 for detailed line profiles for these transitions). In order to be detectable, EWs $\gtrsim 5$ Åare required, which are only reached for inclination $i \gtrsim 60° - 70°$.

The reason for this behaviour is simply that the wind emanates from an accretion disk. For such an outflow, the highest densities will always be found near the disk plane. As the wind accelerates and expands away from the disk, its density must drop to maintain mass continuity. Equatorial sightlines close to the disk plane therefore encounter more material, even though the outflow itself is not preferentially focused in this direction.

4.2 Mass-loss Rates

The wind mass-loss rates ($\dot{M}_{wind,outer}$) listed in Table 1 increase as the luminosity of the central source increases. However, when we compare these values to the implied accretion rate ($\dot{M}_{acc}$) onto the central object (assuming the same 8.3% efficiency as in H18), we find that $\dot{M}_{wind,outer} \simeq 2\dot{M}_{acc}$ for all cases. This 'wind efficiency' is similar to what was found in the quasi-analytic calculations carried out by Done et al. (2018) when considering comparable disk sizes and Compton temperatures. Specifically, they found a peak efficiency of $\dot{M}_{wind,outer} \simeq 2\dot{M}_{acc}$ at luminosities close to the lowest we consider. The wind efficiency then decreases slowly with luminosity in their calculations, but always remains greatyre than unity. In general, the wind efficiencies in our RHD simulations are slightly larger than theirs. This is interesting since we neglect any radiation driving effects, which they include via an approximate correction.

Observationally inferred wind efficiencies have been compiled and presented by Ponti et al. (2012), and it is instructive to compare our results to these. Figure 4 shows this comparison, with the black symbols referring to the observations and the red stars showing the results of our simulations.

At first sight, our prediction of roughly constant wind efficiency does not appear to agree with the observations. However, the apparent increase in the observationally inferred wind efficiency with luminosity is driven entirely by multiple observations of a single source – GRS 1915+105 – at the highest luminosities, $L \gtrsim 0.5 L_{Edd}$. In this regime, radiation pressure – which is neglected in our simulations – is likely to be important (see above and Section **??**). Moreover, even by the standards of XRBs, GRS 1915+105 is exceptional. First, it has been accreting at a significant fraction of the Eddington limit ever since its discovery in 1992 (Castro-Tirado et al. 1994; Court et al. 2017). Second, it exhibits extremely unusual spectral states and variability properties (Zoghbi et al. 2016, e.g.), quite different from the canonical low/hard and high/soft states seen in most XRBs. Third, with an orbital period of 34 days (Casares & Jonker 2014), it is by far the largest known XRB system and could therefore host a signficantly larger accretion disk than we include in our model.

Given all this, we do not think it is possible to make a meaningful comparison between our simulations and (at least) the highest luminosity observations of GRS 1915+105. At more moderate luminosities, we find reasonable agreement between models and observations over roughly an or-
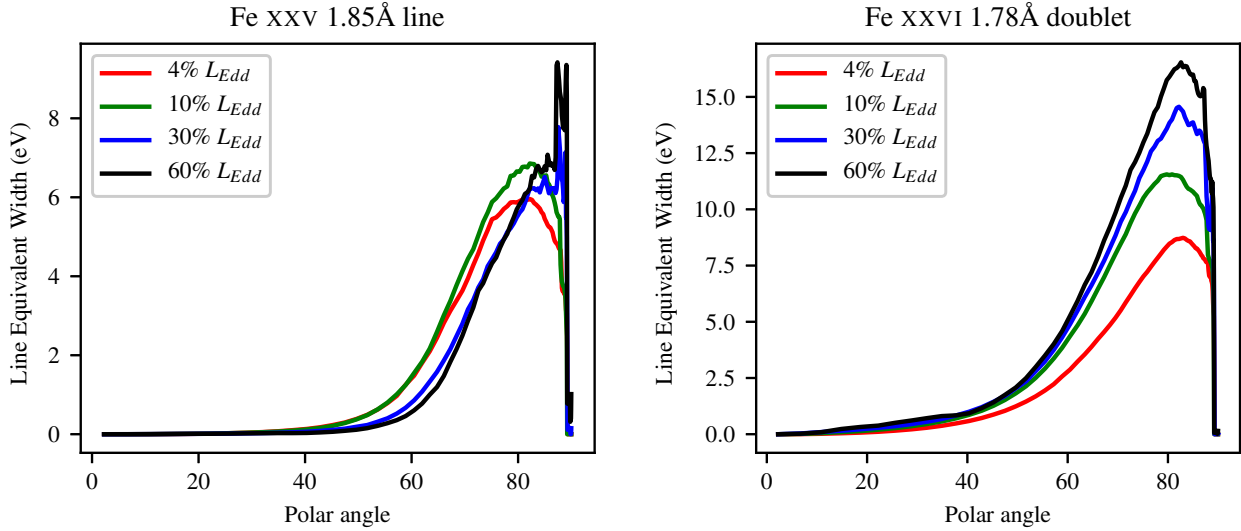
Figure 3. The orientation dependence of the wind-formed Fe XXV (1.85 Å) and Fe XXVI Lyman α (1.85 Å) resonance lines in our simulations. Even though the *mass loss* quasi-spherical (see Figure 3), *detectable absorption lines* are only expected for equatorial sight lines, in agreement with observations.
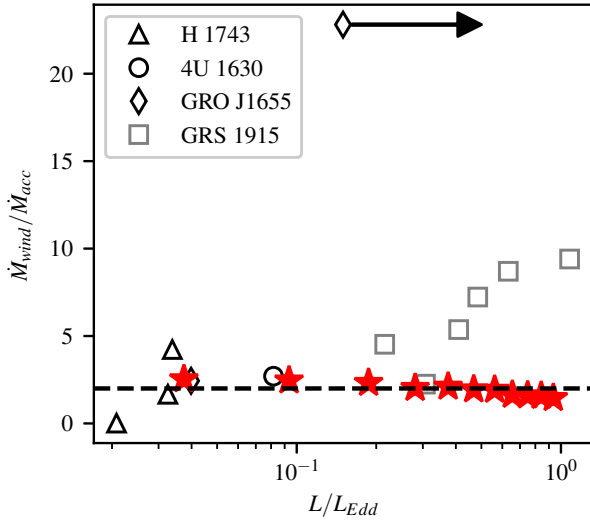

Figure 4. $\dot{M}_{wind}/\dot{M}_{acc}$ vs. luminosity based upon figure 5 in Ponti et al. (2012). Black symbols are empirical values obtained from *Chandra* HETG data for several LMXBs. The red stars represent the results of the simulations presented here, and the dotted line is at $\dot{M}_{wind}/\dot{M}_{acc}=2.0$.

der of magnitude in luminosity, $0.02 \, L_{Edd} \gtrsim L \gtrsim 0.3 \, L_{Edd}$. Across this range, the wind efficiency is consistent with remaining roughly constant at $\dot{M}_{wind}/\dot{M}_{acc} \simeq 2.0$.

4.3   X-ray Absorption Lines

In order to allow a more direct comparison to obervations, we have also computed synthetic X-ray absorption line profiles for our simulations. These are calculated using the

ray-tracing technique described in Higginbottom & Proga (2015).

In Figure 5, we show the dependence of the Fe XXV Lyman α transition at 1.85 Å (6.7 keV) on luminosity, for a representative high-inclination sightline of 80°. Since the line is always saturated, the overall equivalent width (EW) remains fairly constant, at about 5-6 eV. However, the blue edge of the absorption profiles moves to higher velocities with increasing luminosity, in line with the faster outflow speeds seen at higher luminosities in our simulations.

There is also a notable difference between the line profiles produced by the two lower-luminosity simulations, and those calculated from the two higher-luminosity ones. All four models produce significant absorption at the rest wavelength of the line and at red shifts up to about $v \simeq +100 \, kms^{-1}$. This is due to the thermally broadened line profile associated with stationary or slow-moving material in the outflow. In the two low-luminosity simulations – i.e. for $L \lesssim 0.2 \, L_{Edd}$ – this features is almost black at $v \simeq 0 \, kms^{-1}$. By contrast, in the two higher luminosity simulations with $L \gtrsim 0.2 \, L_{Edd}$, saturation only sets in around $v \simeq -100 \, kms^{-1}$.

This weakening of zero velocity absorption features is due to the increased heating rate associated with higher luminosities. In a thermally driven wind, $v_{wind} \simeq v_{thermal}$, so the outflow velocity at any point in the wind is effectively set by the local temperature. Stronger heating therefore produces higher velocities, which is consistent with the disappearance of low-velocity absorbing material at higher luminosities.

But why is there an apparent step-change in the line profile shape around $L \simeq 0.2 \, L_{Edd}$? As already noted by Begelman et al. (1983), one useful way to classify thermally driven winds is by considering the local heating and dynamical time-scales, t_H and t_{dyn}, respectively, in the acceleration zone. If $t_H << t_{dyn}$, gas is heated impulsively and accelerates quickly. If $t_H >> t_{dyn}$, the outflow is heated steadily as
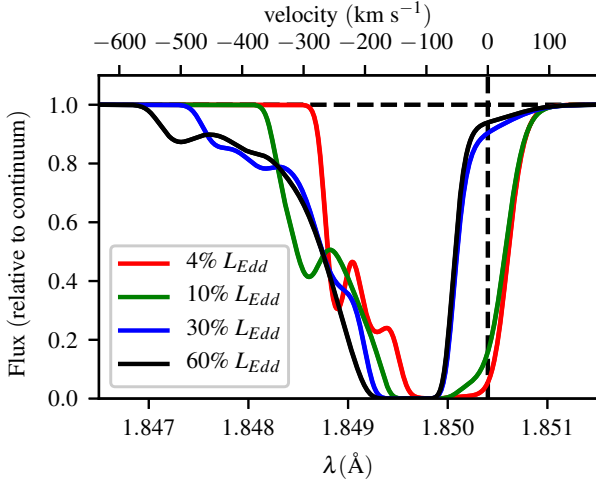
Figure 5. Simulated line profile for the Fe XXV Lyman α transition at 1.85 Å, as viewed from $i = 80°$ for a range of luminosities.

Figure 6. Simulated line profile for the Fe XXVI Lyman α doublet, as viewed from $i = 80°$ for a range of luminosities (thin lines) and also smoothed with a Gaussian to represent the appearance when observed with the *Chandra* HETG with a resolution of 0.012 Å (thick lines)

it rises above the disk and also accelerates more gradually. The critical luminosity at which $t_H \simeq t_{dyn}$ is expected to be

$$L_{crit} \simeq 2 \times 0.03 T_{C,8}^{-1/2} L_{Edd}, \qquad (2)$$

where $T_{C,8}$ is the Compton temperature in units of $10^{8°}$, and the factor of two on the right-hand side is based on the calculations of (Woods et al. 1996, hereafter W96). Since $T_C = 1.4 \times 10^7$ K for our adopted SED, $L_{crit} \simeq 0.16 L_{Edd}$ in our simulations. This is close to the luminosity where the zero-velocity absorption feature disappears in our synthetic line profiles.

Another feature that is commonly seen in XRB winds is the Fe XXVI Lyman α resonance line at 1.8 Å. This is actually a doublet, with components at 1.778 Å (6.973 keV) and 1.783 Å (6.952 keV). Figure 6 shows the synthetic absorption lines for this feature. The velocity-dependent line profile shape of each doublet component is almost identical to that of the Fe XXV feature in Figure 5. However, since these transitions are slightly less saturated, they exhibit a larger dynamic range in EW, ranging from -8 eV for L = 0.04 L_{Edd} to -16 eV for L = 0.6 L_{Edd}. The absorption line obtained from the L = L_{Edd} simulation has an EW of almost 20 eV. However, this should be treated with caution because of the lack of radiation driving in our simulation.

The current generation of X-ray spectrometers are generally unable to resolve this doublet. For example, the wavelength resolution of the first-order spectrum provided by the *Chandra* HETG is 0.012 Å, compared to the double separation 0.005 Å. [2] The thick lines in Figure 6 illustrate the effect of convolving the synthetic spectrum with a Gaussian representing the first-order *Chandra* HETG line-spread function.

The presence of detectable Fe XXV and Fe XXVI features in our synthetic spectra is promising. However, do the properties of these features – their strength and width/blueshift – match observations *quantitatively*? The observed EWs of Fe XXV and Fe XXVI absorption lines in XRBs are typically in the range of 10-30 eV Ponti et al. (2012). This is comparable to the values we measure in our synthetic spectra. However, the outflow velocities inferred from the observed absorption lines are typically 100-3000 km s^{-1} Díaz Trigo & Boirin (2016); Ponti et al. (2016). This range extends to significantly higher speeds than are found in our simulations.

Part of the reason for this discrepancy may be continuum driving. Especially for luminosities approaching L_{Edd}, this is likely to accelerate material to higher velocities, but is neglected in our RHD calculations. Higher wind speeds would also tend to increase the predicted EWs, since they help to desaturate the line profile by spreading the opacity over a larger velocity range. Finally, there is some evidence that the observed absorption lines contain contributions from multiple (low- and high-velocity) absorption "zones" Miller et al. (2015). If so, then thermally driven outflows may be associated specifically with the low-velocity absorbers.

4.4 Kinetic Luminosity

The kinetic luminosity carried by the disc wind is astrophysically important for two reasons. First, it represents a potentially significant non-radiative sink for the available accretion luminosity. Second, it provides a measure of the likely impact of the outflow on its surroundings. We therefore estimate the kinetic luminosity of the disc winds in our RHD simulations by summing $\frac{1}{2}\dot{M}_i v_{R,i}$ around the outer edge of our grid. Here, $\dot{M}_i$ and $v_{R,i}$ are the mass-loss rate through, and radial velocity in, a particular grid-cell i that lies on

---

[2] It is worth noting that (Miller et al. 2015) and Miller et al. (2016) were able to extract meaningful *third-order* spectra from *Chandra* observations of a few bright XRBs. In some of these, the Fe XXVI doublet is, in fact, (marginally) resolved.
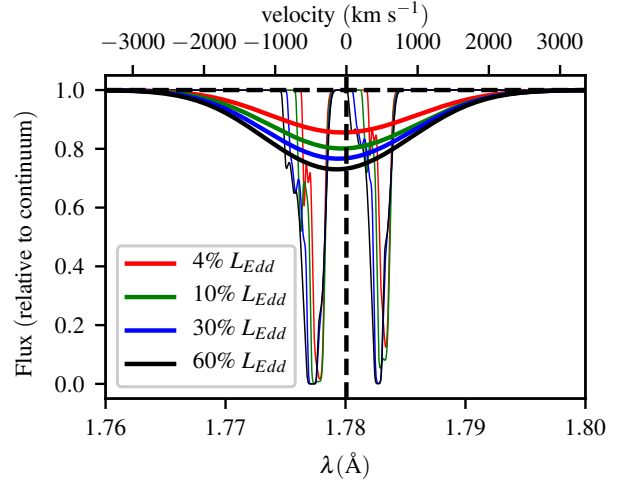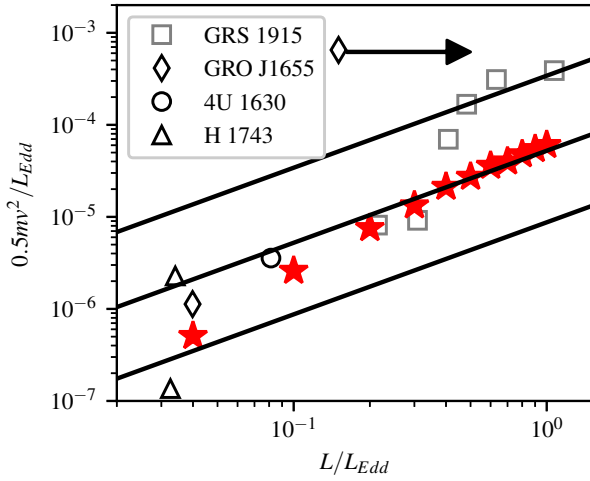
Figure 7. Kinetic energy transported by the wind as a function of source luminosity, both normalised to the Eddington luminosity. Crosses are for this work, the other symbols represent date from Ponti et al. (2016), the symbols code for different sources as in Figure 4. The diagonal lines show theoretical calculations of kinetic luminosity assuming a 0.1 per cent conversion from luminosity to kinetic energy for disks with $1°$, $6°$ and $40°$ total flare.

this edge. The resulting kinematic luminosities are shown in Figure 7 as a function of L_x, along with observationally inferred values taken from (Ponti et al. 2016), for the same sources shown in Figure 4.

Fundamentally, thermally driven winds in XRBs are driven by the conversion of the X-ray luminosity intercepted by the accretion disk into the kinetic luminosity of the outflowing gas. Following (Ponti et al. 2016), we therefore also include in 7 lines corresponding to a constant efficiency of conversion, assuming flared disks with fixed opening angles or $1°$, $6°$ and $40°$.

In our simulations, the hydrostatic "disk" near $z = 0$ has an opening angle of is $\simeq 4°$ for low luminosities, rising to $\simeq 6°$ for the $L = L_{Edd}$ run. Based on this, we estimate the conversion efficiency to be $\simeq 0.1\%$ at $L \geq 0.2 L_{Edd}$. In the two lower luminosity runs, the efficiency is lower, $\simeq 0.04$ per cent at $0.04 L_{Edd}$ and $\simeq 0.06$ per cent at $0.1 L_{Edd}$. Interestingly, these are again the two runs for which $L \lesssim L_{crit}$ (c.f. Section 4.3).

It is worth re-emphasizing here that our RHD simulations are explicitly designed to *not* capture the entire hydrostatic disk atmosphere. Thus the geometric flaring of the wedge of cool, quasi-static gas near $z = 0$ is not due to the usual convex structure of hydrostatic α-disks. Instead, as discussed in , the disk opening angle in our simulations is driven by the radial dependence of the depth to which X-rays emitted by the central object can penetrate.

In reality, therefore, the true opening angle might be larger than in the simulations. In addition, it has been shown that at high Eddington fractions, accretion disks tend to puff up to yet larger scale heights (Abramowicz et al. 1988; Okuda et al. 2005, but also see Lasota et al. 2016). We may therefore expect real disks – especially in high-luminosity

XRBs – to intercept a greater fraction of the incoming radiation. This might explain why the observed kinetic energy flux appears to increase significantly for $L \geq 0.3 L_{Edd}$. If the outflows at these luminosities are thermally driven, with the same efficiency as those at lower luminosities, the implied disk opening is $\simeq 40°$. However, in this high luminosity regime, radiation driving may also help to increase the conversion efficiency.

4.5 Radiative Driving

At luminosities approaching L_{Edd}, radiation pressure will become increasingly important. In general, we expect the plasma above the disk to by largely ionized, so the momentum transfer between photons and plasma will be dominated by electron scattering. The net effect is effectively a reduction in the Compton radius, i.e. the innermost radius from which a thermal wind can be launched. Done et al. (2018) estimate this reduction to be

$$\overline{R}_{IC} \to R_{IC}\left(1 - \frac{L}{0.71 L_{Edd}}\right), \qquad (3)$$

which means that the wind can be launched from all radii once $L \geq 0.71 L_{Edd}$.

Since we neglect radiative driving, the mass-loss rates we estimate from our RHD simulations are, strictly speaking, lower limits for luminosities approaching or exceeding this value. However, we can make a rough estimate of the expected size of this effect. In our two highest luminosity runs ($L = 0.6 L_{Edd}$ and $L = L_{Edd}$), the mass-loss rate per unit area from the disk is approximately proportional to $R^{-1.5}$. If all the radii interior to where the wind current arises were to follow this relationship, the total mass-loss rate would increase by a factor of about 1.5. We might also expect somewhat higher velocities in the outflow, due to the additional driving force. As noted above, this, in turn, would then also increase the efficiency with which radiative luminosity is converted into kinetic luminosity.

5 SUMMARY

Thermal driving is an attractive mechanism to explain the outflows observed in several X-ray binaries seen at high inclinations. We have previously demonstrated via radiation-hydrodynamic simulations that the outflow seen in the soft-intermediate state of GRO J1655-40 can be plausibly modelled as a thermal wind driven by X-ray irradiation. Here we extend these simulations to higher X-ray luminosities in order to test the viability of this mechanism more generally. Our main findings are:

- The mass-loss rate associated with the thermally driven disk winds in our RHD simulations scale roughly linearly with X-ray luminosity (and hence accretion rate). Thus he *efficiency* of these outflows is roughly constant, at $\dot{M}_{wind}/\dot{M}_{acc} \simeq 2$. This agrees with previous theoretical studies and is also in line with observations.

- Thermally driven disk winds are *not* intrinsically equatorial, but rather quasi-spherical. However, since the wind densities are highest near the disk plane, the highest *columns* – and detectable absorption lines – are only found for high-inclination sightlines, $i \gtrsim 60° - 70°$. This is consistent with

observations. Thus the absence of wind-formed absorption lines from the spectra of low-inclination XRBs does *not* require an equatorial outflow geometry.

• The speed of our simulated outflows increases with luminosity, as do the blueshifts of the Fe xxv and Fe xxvi absorption lines we have calculated for them.

• The kinetic energy carried by the outflow also increases with luminosity. The efficiency with which radiative luminosity is converted to kinetic luminosity in our simulations is ≃0.1 per cent. However, this efficiency depends on both the flare angle of the disk and radiation pressure, neither of which are self-consistently accounted for in our simulations.

REFERENCES

Abramowicz M. A., Czerny B., Lasota J. P., Szuszkiewicz E., 1988, ApJ, 332, 646
Allen J. L., Schulz N. S., Homan J., Neilsen J., Nowak M. A., Chakrabarty D., 2018, ApJ, 861, 26
Aranzana E., Scaringi S., Körding E., Dhillon V. S., Coppejans D. L., 2018, MNRAS, 481, 2140
Begelman M. C., McKee C. F., Shields G. A., 1983, ApJ, 271, 70
Bu D.-F., Yang X.-H., 2018, MNRAS, 476, 4395
Casares J., Jonker P. G., 2014, Space Sci. Rev., 183, 223
Castor J. I., Abbott D. C., Klein R. I., 1975, ApJ, 195, 157
Castro-Tirado A. J., Brandt S., Lund N., Lapshov I., Sunyaev R. A., Shlyapnikov A. A., Guziy S., Pavlenko E. P., 1994, ApJS, 92, 469
Court J. M. C., Altamirano D., Pereyra M., Boon C. M., Yamaoka K., Belloni T., Wijnands R., Pahari M., 2017, MNRAS, 468, 4748
Díaz Trigo M., Boirin L., 2016, Astronomische Nachrichten, 337, 368
Done C., Tomaru R., Takahashi T., 2018, MNRAS, 473, 838
Dyda S., Dannen R., Waters T., Proga D., 2017, MNRAS, 467, 4161
Falcke H., Körding E., Markoff S., 2004, A&A, 414, 895
Fender R., Belloni T., 2012, Science, 337, 540
Gayley K. G., 1995, ApJ, 454, 410
Higginbottom N., Proga D., 2015, ApJ, 807, 107
Higginbottom N., Knigge C., Long K. S., Sim S. A., Matthews J. H., 2013, MNRAS, 436, 1390
Higginbottom N., Proga D., Knigge C., Long K. S., 2017, ApJ, 836, 42
Higginbottom N., Knigge C., Long K. S., Matthews J. H., Sim S. A., Hewitt H. A., 2018, MNRAS, 479, 3651
Homan J., Neilsen J., Allen J. L., Chakrabarty D., Fender R., Fridriksson J. K., Remillard R. A., Schulz N., 2016, ApJ, 830, L5
Kallman T. R., Bautista M. A., Goriely S., Mendoza C., Miller J. M., Palmeri P., Quinet P., Raymond J., 2009, ApJ, 701, 865
Körding E. G., Jester S., Fender R., 2006, MNRAS, 372, 1366
Körding E., Rupen M., Knigge C., Fender R., Dhawan V., Templeton M., Muxlow T., 2008, Science, 320, 1318
Lasota J.-P., Vieira R. S. S., Sadowski A., Narayan R., Abramowicz M. A., 2016, A&A, 587, A13
Long K. S., Knigge C., 2002, ApJ, 579, 725
Luketic S., Proga D., Kallman T. R., Raymond J. C., Miller J. M., 2010, ApJ, 719, 515
Maccarone T. J., Gallo E., Fender R., 2003, MNRAS, 345, L19
Matthews J. H., Knigge C., Long K. S., Sim S. A., Higginbottom N., 2015, MNRAS, 450, 3331
Miller J. M., Raymond J., Fabian A., Steeghs D., Homan J., Reynolds C., van der Klis M., Wijnands R., 2006, Nature, 441, 953
Miller J. M., Raymond J., Reynolds C. S., Fabian A. C., Kallman T. R., Homan J., 2008, ApJ, 680, 1359
Miller J. M., Fabian A. C., Kaastra J., Kallman T., King A. L., Proga D., Raymond J., Reynolds C. S., 2015, ApJ, 814, 87
Miller J. M., et al., 2016, ApJ, 821, L9
Netzer H., 2006, ApJ, 652, L117
Nowak M. A., 1995, PASP, 107, 1207
Okuda T., Teresi V., Toscano E., Molteni D., 2005, MNRAS, 357, 295
Owen J. E., Clarke C. J., Ercolano B., 2012, MNRAS, 422, 1880
Park S. Q., et al., 2004, ApJ, 610, 378
Ponti G., Fender R. P., Begelman M. C., Dunn R. J. H., Neilsen J., Coriat M., 2012, MNRAS, 422, 11
Ponti G., Bianchi S., Muñoz-Darias T., De K., Fender R., Merloni A., 2016, Astronomische Nachrichten, 337, 512
Proga D., Stone J. M., Kallman T. R., 2000, ApJ, 543, 686
Scaringi S., 2014, MNRAS, 438, 1233
Scaringi S., Körding E., Uttley P., Knigge C., Groot P. J., Still M., 2012, MNRAS, 421, 2854
Scaringi S., Körding E., Groot P. J., Uttley P., Marsh T., Knigge C., Maccarone T., Dhillon V. S., 2013, MNRAS, 431, 2535
Scaringi S., et al., 2015, Science Advances, 1, e1500686
Shakura N. I., Sunyaev R. A., 1973, A&A, 24, 337
Shidatsu M., Done C., Ueda Y., 2016, ApJ, 823, 159
Shields G. A., McKee C. F., Lin D. N. C., Begelman M. C., 1986, ApJ, 306, 90
Sobczak G. J., McClintock J. E., Remillard R. A., Bailyn C. D., Orosz J. A., 1999, ApJ, 520, 776
Stone J. M., Norman M. L., 1992, ApJS, 80, 753
Uttley P., Klein-Wolt M., 2015, MNRAS, 451, 475
Uttley P., McHardy I. M., 2001, MNRAS, 323, L26
Van de Sande M., Scaringi S., Knigge C., 2015, MNRAS, 448, 2430
Woods D. T., Klein R. I., Castor J. I., McKee C. F., Bell J. B., 1996, ApJ, 461, 767
Zoghbi A., et al., 2016, ApJ, 833, 165
()

This paper has been typeset from a TeX/LaTeX file prepared by the author.